Chapter 5

High-rate performance of H_xMoO_3 for aqueous aluminium-ion battery

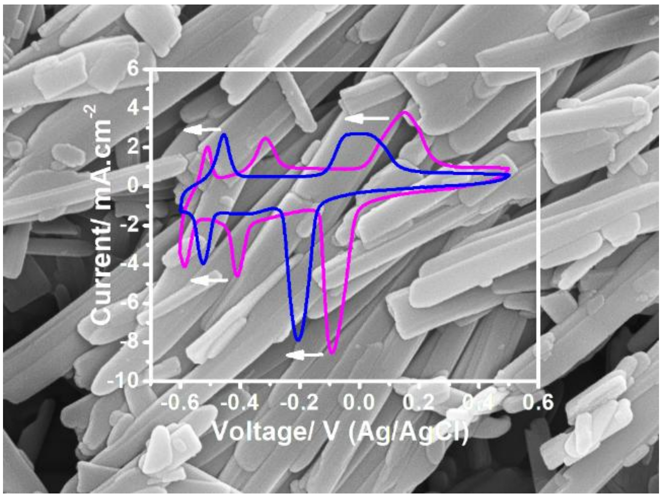

Herein, the electrochemical Al^{3+} ion storage behavior in H_xMoO_3 in aqueous electrolyte is illustrated which underscores the influence of H doping in significantly enhancing the specific capacities and long-term cycling stability even at very high current rates.

Ref.: R. Baishya, K. Roy, and S. K. Das, "High-rate performance of H_xMoO_3 for aqueous aluminium-ion batteries," Chemical Communications, vol. 61, no. 44, pp. 8031–8034, 2025.

5. High-rate performance of H_xMoO_3 for aqueous aluminium-ion battery

5.1 Introduction

As discussed in the introduction chapter, it is well known that a quintessential component for high performance rechargeable metal-ion batteries are robust electrodes which can sustain ultralong life while also delivering reasonably high energy density [1-5]. Graphite, having a theoretical capacity of 372 mAhg^{-1} for Li^+ ion storage, is one of the most spectacular anode materials ever found for Li-ion batteries [6]. The electrochemistry of various transition metal oxides is also extensively explored for possible application in rechargeable batteries [7]. One such extraordinary metal oxide is molybdenum trioxide (MoO_3). The theoretical capacity exhibited by MoO_3 is 1117 mAhg^{-1} which is almost three times higher than graphite [8,9]. It is reported that various forms of pristine MoO_3 can display Li^+ ion discharge capacities in the range of 200 - 1100 mAhg^{-1} at current rates range of 300 – 5000 mAg^{-1} with discharge and charge potential plateaus at 2.25 V and 2.6 V (vs Li) [10,11]. The high current performance is also very impressive with specific capacities reaching as high as 554 mAhg^{-1} at current rate of 5000 mAg^{-1} [12,13]. The Li^+ ion storage mechanism generally shows conversion of MoO_3 to Li_xMoO_3 and further to metallic Mo and Li_2O [14,15]. Similarly, there are extensive studies on Na^+ ion storage [16,17]. Most of these electrochemical investigations are pursued keeping in mind the applicability of MoO_3 in non-aqueous systems. However, considering the dual benefit of enhanced safety and reduced cost, electrochemical energy storage systems with aqueous electrolytes are also worth exploring [18]. It may not be a straightforward approach to directly translate electrode materials known for its electrochemical redox activity in non-aqueous systems to aqueous counterpart due to the very limital electrochemical potential window of aqueous electrolyte [19]. In this regard, MoO_3 may be a very promising material. A rocking chair type aqueous battery with Al^{3+} ion as the primary charge carrier will be an excellent addition in the family of ‘beyond Li-ion’ rechargeable metal-ion batteries. There are reports which illustrate that MoO_3 shows good Al^{3+} ion storage behavior [20,21]. But MoO_3 faces capacity retention issues at high current rates. Doping is a simple yet powerful strategy found to be exceptionally successful in influencing the Li^+/Na^+ ion storage kinetics in Li^+/Na^+ ion-batteries [22,23]. Therefore, the doping strategy has been employed on MoO_3 to understand its effect on Al^{3+} ion storage. Benefiting from various spectroscopic, microscopic and electrochemical outcomes, it is shown that H doping significantly improves the high-rate performance of MoO_3.

5.2 Experimental Section

5.2.1 Materials

Ammonium heptamolybdate tetrahydrate ($(NH_4)_6Mo_7O_{24}.4H_2O$), hydrochloric acid (HCl), lithium manganese oxide ($LiMn_2O_4$), distilled water.

5.2.2 Synthesis

A simple facile hydrothermal technique was used to prepare MoO_3 as outlined in reference [24]. All the chemical reagents are analytical grade and they are used without further purification. In short, 0.6 g of ammonium heptamolybdate tetrahydrate ($(NH_4)_6Mo_7O_{24}.4H_2O$) was firstly dissolved in 36 ml of deionized water followed by continuous stirring. Then a very small amount (1 ml) of hydrochloric acid (HCl) was added slowly in the previous solution followed by stirring for 5 minutes. The final solution mixture was then transferred to a 50 ml Teflon lined autoclave and heated for 160 °C for 15 h. After that the solution was cooled naturally followed by washing with distilled water and ethanol. The obtained precipitate was dried at 90 °C for 24 hour and the final product was procured. A similar kind of procedure was followed to obtain the hydrogen dopped H_xMoO_3 wherein the volume of HCl was increased to 3.5 ml to facilitate enhanced doping keeping the other parameters same.

5.2.3 Characterization

The phase identification and the purity assessment of the as prepared samples were performed using X- ray diffraction (BRUER AXS D8 FOCUS, Cu-K_α radiation; λ= 1.5406 Å) and Raman spectroscopy (RENISHAW BASIS SERIES WITH 515 LASER, RENISHAW, UK). The morphology of the two samples were comprehensively analyzed with the FESEM images. X-ray photoelectron spectroscopy is performed to understand the formation of hydrogen dopped H_xMoO_3. High Score Plus 3.0d (3.0.4) software is used to index the crystallographic details.

5.2.4 Electrochemical analysis

The fabrication of the working electrode for electrochemical and morphological analysis was performed by preparing electrode slurries of active materials (MoO_3 and H_xMoO_3), carbon black and polyvinylidene fluoride in a weight ratio of 7:2:1 using N-methyl-2-pyrrolidone as solvent. The obtained slurry was cast on graphite current collector and it was dried for 12 hours at 90^o C.

The electrochemical activities of the MoO_3 and H_xMoO_3 were evaluated using cyclic voltammetry and galvanostatic charge discharge experiments in a three-electrode glass cell set up where Pt electrode and the Ag/AgCl electrode was used as counter and reference electrode respectively. The cyclic voltammetry analysis was conducted within a potential window of -0.6 V to 0.5 V (vs Ag/AgCl) at different scan rates. Similarly, the charge-discharge profiles for both the materials were procured within the same voltage range as CV measurements in current densities ranging from 2 Ag^{-1} to 20 Ag^{-1}. The electrolytes used here were of various concentration of $AlCl_3$ and $Al_2(SO_4)_3$. The EIS was performed for both the materials in 1 M $AlCl_3$ aqueous electrolyte in the frequency range of 1 mHz to 200 kHz with a signal amplitude of 10 mV.

Calculation of Diffusion coefficient

From EIS:

The Diffusion coefficient ($D_{Al^{3+}}$) can be estimated from the following Equation (Ref. 19, 20):

$$D_{Al^{3+}} = 0.5\left(\frac{RT}{An^2F^2C\sigma_w}\right)^2$$

where R is the gas constant (8.314 J mol^{-1} K^{-1}), T is the absolute temperature (298.15 K), A is the surface area of the electrode (0.25 cm^2), n is the number of electrons transferred, F is Faraday constant (96500 C mol^{-1}), C is the concentration of Al^{3+} ion in the solution (1 M), and σ_W is the Warburg coefficient, calculated by the following Equation (at low-frequency region).

$$Z' = R_S + R_{CT} + \sigma_W\, \omega^{-0.5}$$

where R_S depicts electrolyte resistance, R_{CT} is the charge transfer resistance, σ_w can be obtained from the slope of linear fitting of the real part of impedance (Z′) vs. the reciprocal square root of angular frequency ($\omega^{-0.5}$). The linear fitting is shown in figure 5.20 below.

From GITT:

The diffusion coefficient is estimated using the formula (Ref. 36):

$$D_{Al^{3+}} = \frac{4}{\tau\pi}\left(\frac{iV}{zFS}\right)^2\left(\frac{\Delta E_s}{\Delta E_t}\right)^2$$

Where i is the current (A); V_m is the molar volume of the electrode (cm^3/mol); z is the charge number; F is the Faraday's constant (96485 C/mol), and S is the electrode area (cm^2). ΔE_s corresponds to steady state voltage change and ΔE_s corresponds to voltage change during constant current pulse by single titration curve during discharge eliminating the iR drop. Here in the electrodes were discharged at a constant current density of 0.1 $mAcm^{-2}$ followed by an open circuit relaxation of 1 minute to allow the cell in order to reach its steady state value. The operating voltage window was similar to the previous electrochemical measurements i.e from -0.6 V to 0.5 V.

5.4 Results and Discussion:

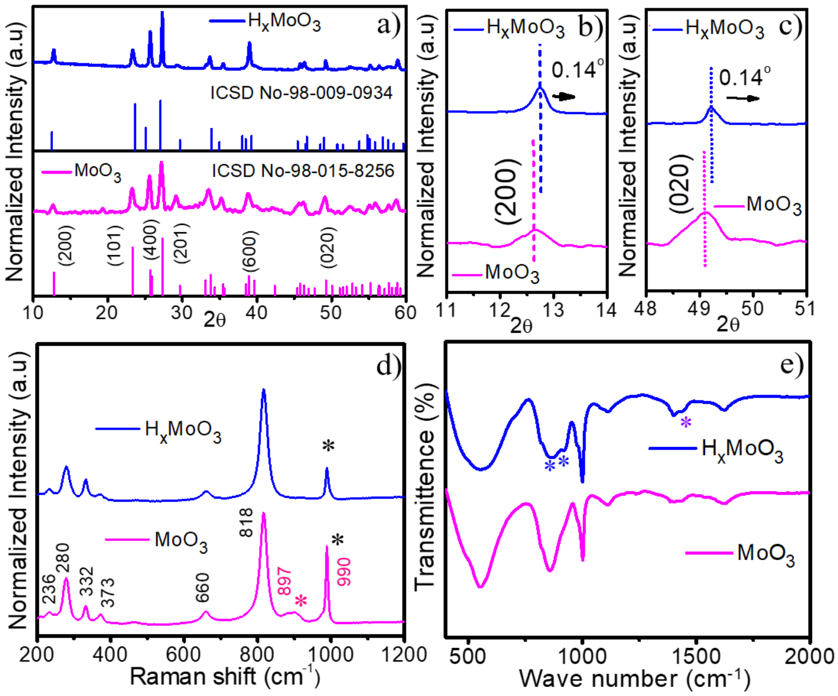

Figure 5.1 (a-c) XRD analysis, (d) Raman spectra, (e) FTIR spectra of MoO_3 and H_xMoO_3.

MoO_3 and H doped MoO_3 (H_xMoO_3) were synthesized hydrothermally. The crystalline forms of the materials were identified using powder XRD analysis (Figure 5.1(a-c)). It indicates that both the materials are crystallized in the orthorhombic phase (ICSD no 98-009-0934 & 98-015-8256). The x content in H_xMoO_3 is 0.28 as per crystallographic data. Raman spectra of MoO_3 and H_xMoO_3 exhibit the generally observed characteristic bands of MoO_3 (Figure 5.1d and table 5.1). However, subtle differences could be noticed in case of H_xMoO_3. For example, the band positioned at 897 cm^{-1} is vanished in H_xMoO_3. A normalized comparison indicates reduction of the intensity of the peak positioned at around 995 cm^{-1}. This may be interlinked with the possible interaction of the doped hydrogen with the terminal oxygen. These changes indicate a potential alteration in the material's electronic and vibrational structure due to the incorporation of hydrogen atom into the MoO_3 lattice [25]. Similarly, few minute differences could be noticed from the FTIR analysis of MoO_3 and H_xMoO_3 also (Figure 5.1e) [26]. The peak positioned at 990 cm^{-1} which can be attributed to the Mo=O stretching vibrations splits into two distinct peaks in the case of H_xMoO_3 and the peak at 1404 cm^{-1} also splits into two which may signify deformation in the Mo-OH bond deformation [26]. Moreover, an additional peak appears at 920 cm^{-1} alongside the peak at 860 cm^{-1}. These indicate possible changes in the local bonding environment and electronic interactions upon H doping in MoO_3.

Sl no	Peak Position (cm^{-1})	Designation of the band	References (in ESI)
1	995 cm^{-1} 336 cm^{-1}	corresponds to the terminal oxygen (Mo^{6+}=O) stretching mode	2
2	897 cm^{-1}	symmetric stretches of the terminal oxygen	3
3	818 cm^{-1}	the doubly coordinated Mo_2=O bridging oxygen stretching modes	4
4	663 cm^{-1} and 465 cm^{-1}	the triply coordinated Mo_3-O oxygen stretching mode	4
5	200 – 600 cm^{-1}	MoO_3 octahedral bending vibrations and lattice modes	5
6	236 cm^{-1} and 280 cm^{-1}	the bending mode of Mo_2-O and the double bond (Mo=O) vibrations	5
7	373 cm^{-1}	assigned to bending mode of Mo_3-O and Mo=O bending modes	5, 6

Table 5.1. Details of the characteristic Raman peaks observed in MoO_3.

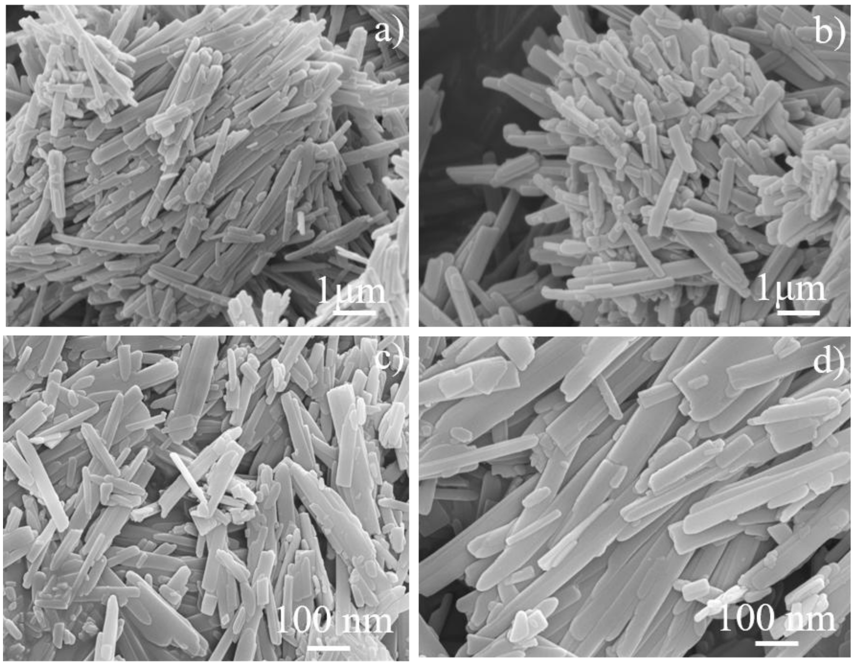

Figure 5.2 FESEM images of (a,b) MoO_3 and (c,d) H_xMoO_3.

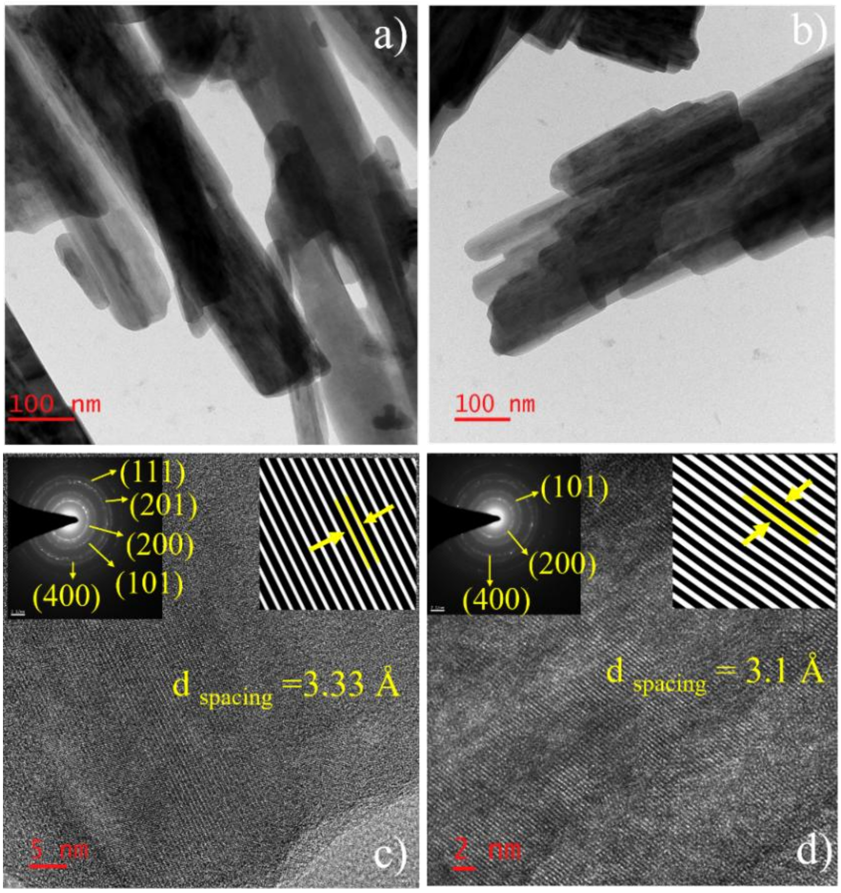

Figure 5.3 TEM images of (a) MoO_3 and (b) H_xMoO_3, HRTEM images, SAED patterns (left inset) and interlayer spacing after processing (right inset) of (c) MoO_3 and (d) H_xMoO_3.

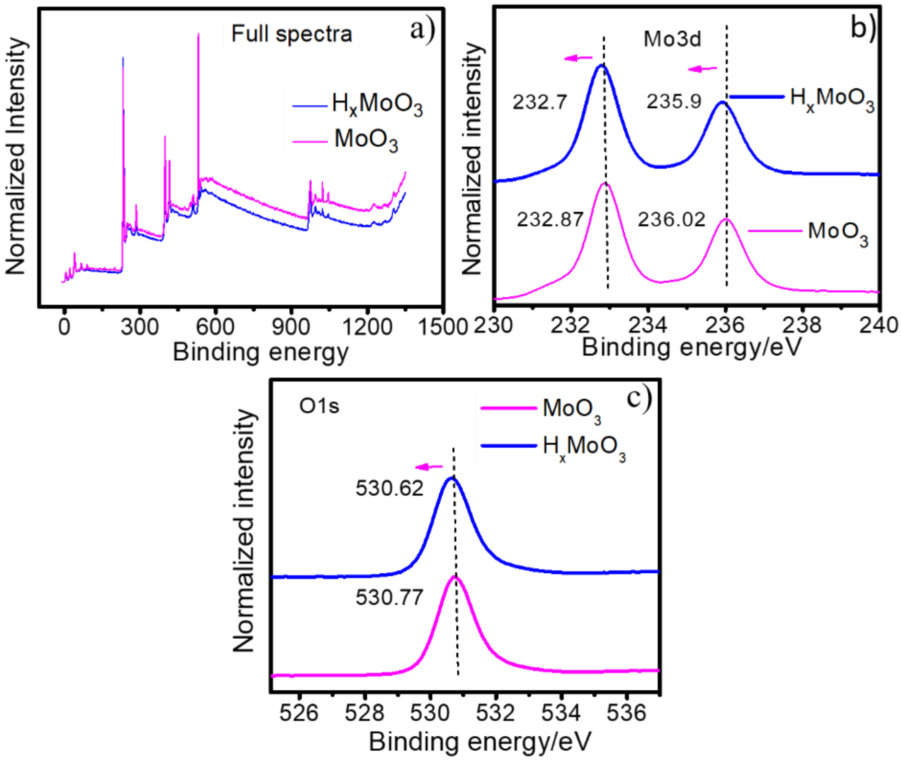

Figure 5.4 a) Full XPS spectra, XPS spectra of b) Mo3d and c) O1s of MoO_3 and H_xMoO_3.

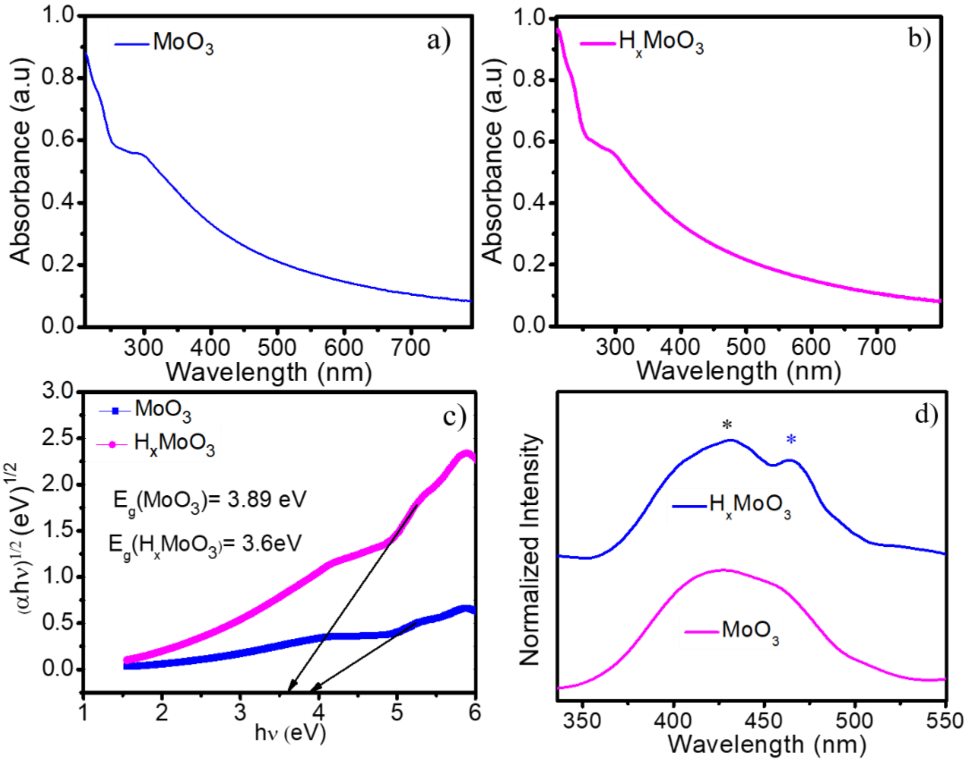

Figure 5.5 UV visible spectra of a) MoO_3 and b) H_xMoO_3; c) Tauc plots obtained from the UV visible data; d) PL spectra of MoO_3 and H_xMoO_3.

MoO_3 and H_xMoO_3 take the shape of nanobelts as per the FESEM and TEM images as shown in Figure 5.2 and 5.3 (c,d). Analysis of HRTEM images and SAED patterns show a fringe width of 3.33 Å for MoO_3 (Figure 5.3c), while it is 3.1 Å for H_xMoO_3 indicating a minor contraction (Figure 5.3d). Supporting this observation, the XRD peaks of H_xMoO_3 also shift to higher angles by 0.14^o (Figure 5.1 (a-c)). Figure 5.4 shows the XPS spectra recorded for the as prepared MoO_3 and H_xMoO_3. The obtained doublets at 232.87 eV and 236.02 eV correspond to the binding energies of Mo $3d_{5/2}$ and Mo 3d3/2 electrons of Mo^{6+} oxidation states for MoO_3 [27-29]. Figure 5.4b shows the binding energies of Mo $3d_{5/2}$ and Mo $3d_{3/2}$ of the hydrogen doped H_xMoO_3 located at 232.7 eV and 235.9 eV. For H_xMoO_3 a slight shift (0.17 eV and 0.12 eV) in the binding energy values can be observed as compared to those for MoO_3. This lowering of binding energy can be correlated with the existence of Mo^{5+} ions in the H_xMoO_3 structure [27,28]. It is a known fact that the binding energy of the core metallic cations reduces under the presence of extra electron [27]. Therefore, it can be inferred that under the influence of hydrogen ion, some molybdenum gets reduced to Mo^{5+} oxidation states and some extra electrons might release. These extra electrons possibly lead to the enhancement in the electrical conductance of H_xMoO_3 [29]. Figure 5.4c shows the O1s binding energy peaks for MoO_3 and H_xMoO_3 located at 530.77 eV and 532.62 respectively [27-29]. A slight shift in the binding energy value can be observed in case of H_xMoO_3. Therefore, considering the presence of different oxidation states of Mo and some moderate binding energy shifts, it can be concluded that hydrogen ion is in the crystal structure of MoO_3. Furthermore, the band gaps (E_g) for both the materials were calculated using the UV-visible data [30]. The estimated E_g values are 3.6 eV for H_xMoO_3 and 3.89 eV for pristine MoO_3 (Figure 5.5 (a-c)). This sort of decrease in the energy band gap value followed by hydrogen insertion may consequently enhance the electronic conductivity. Similarly, there is a slight change in the PL spectra. In the case of pristine MoO_3, there is only one broad emission peak around 430 nm, whereas an additional emission peak at 464 nm could be noticed for H_xMoO_3 (Figure 5.5d). It is related to the generation of oxygen vacancies due to hydrogen doping [31].

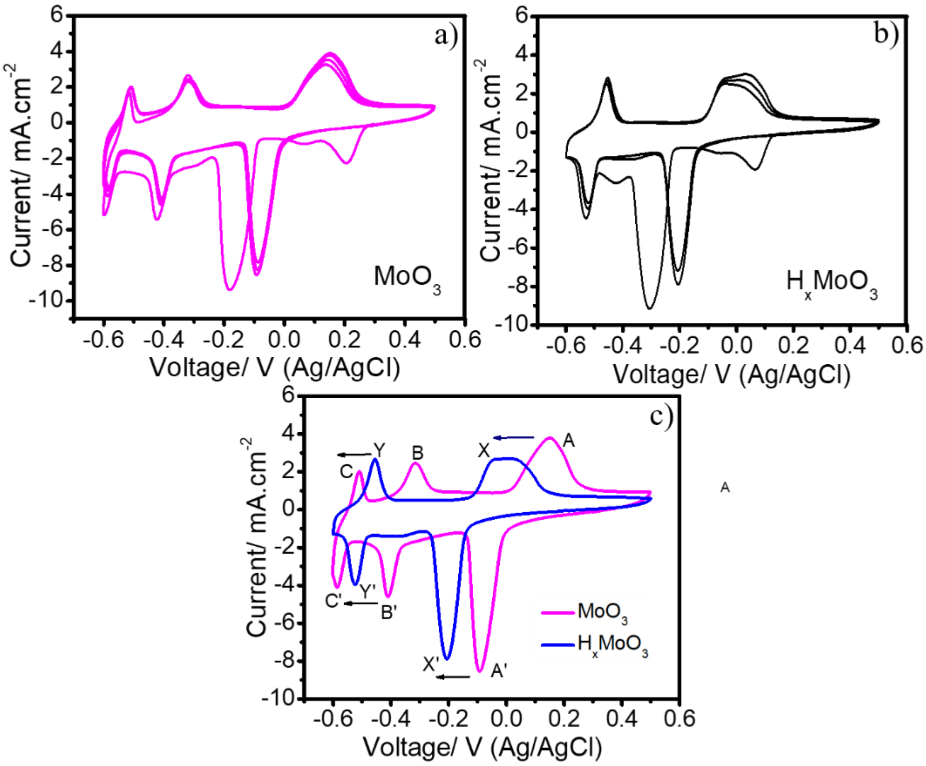

Figure 5.6 Multi-cycle CV curve of (a) MoO_3 and (b) H_xMoO_3, (c) Superimposition of the CV scans of MoO_3 and H_xMoO_3 in aqueous $AlCl_3$ electrolyte at a scan rate of 2.5 mVs^{-1}.

Phases	Electrolyte	Peaks	Peak positions (V)	Peak Separations (V)
MoO_3	1 M $AlCl_3$	A	0.15	0.24
		A’	-0.09	
		B	-0.31	0.27
		B’	-0.4	
		C	-0.5	0.53
		C’	-0.58	
H_xMoO_3	1 M $AlCl_3$	X	-0.01	0.19
		X’	-0.2	
		Y	-0.45	0.07
		Y’	-0.52	
MoO_3	0.5 M $Al_2(SO_4)_3$	E	0.19	0.35
		E’	-0.16	
		F	-0.25	0.22
		F’	-0.47	
H_xMoO_3	0.5 M $Al_2(SO_4)_3$	G	0.13	0.31
		G’	-0.18	
		H	-0.31	0.17
		H’	-0.48	

Table 5.2 Peak to peak separation from Cyclic Voltammetry

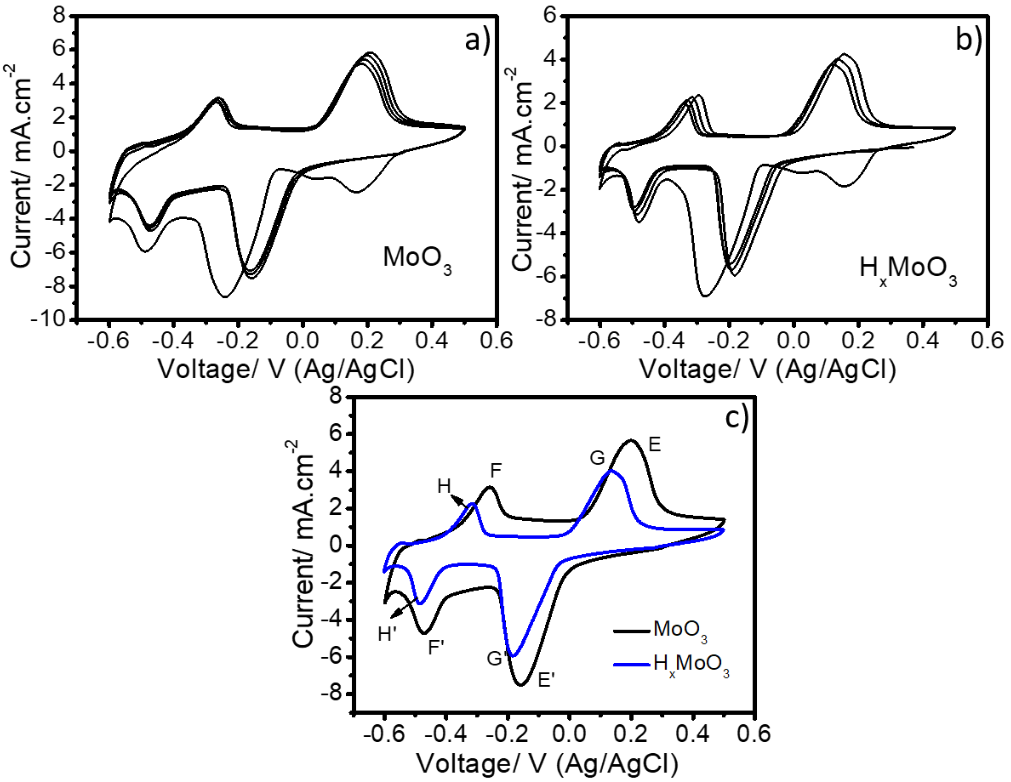

Figure 5.7 CV profile of a) MoO$_3$ and b) H$_x$MoO$_3$, c) Superimposition of the CV scan of MoO$_3$ and H$_x$MoO$_3$ in Al$_2$(SO$_4$)$_3$ aqueous electrolyte at a scan rate of 2.5 mVs^{-1}.

Figure 5.6a and 5.6b show the CV profiles of MoO$_3$ and H$_x$MoO$_3$ in 1 M AlCl$_3$ aqueous electrolyte in the potential range of -0.6 V to 0.5 V at a scan rate of 2.5 mVs^{-1} respectively. In the case of MoO$_3$, there are three sharp cathodic peaks located around -0.09 V, -0.4 V and -0.5 V. The subsequent anodic peaks are positioned at 0.15 V, -0.32 V, -0.5 V (Figure 5.6a). There is however a slight difference in the peak position in the first cathodic cycle. The cathodic peak at -0.182 V that is observed for the first scan is shifted to -0.09 V in the subsequent cycles. It is similar to the already reported data [14a]. On the other hand, the CV profile of H$_x$MoO$_3$ is slightly different (Figure 5.6b). In this case, two sharp cathodic peaks could be seen around -0.23 V and -0.51 V. The peak around -0.4 V which was observed for pristine MoO$_3$ is disappeared. A superimposition of the profiles shows that cathodic and anodic peaks are shifted to more negative side (Figure 5.6c). The most important feature is that there is reduced polarization in the case of H$_x$MoO$_3$. For example, the peak-to-peak separation for peak X and X' is 0.19 V whereas it is 0.24 V for pristine form of MoO$_3$ (between A and A') (Figure 5.6c and Table 5.2). Similar type of differences could also be observed in Al$_2$(SO$_4$)$_3$ aqueous electrolyte (Figure 5.7).

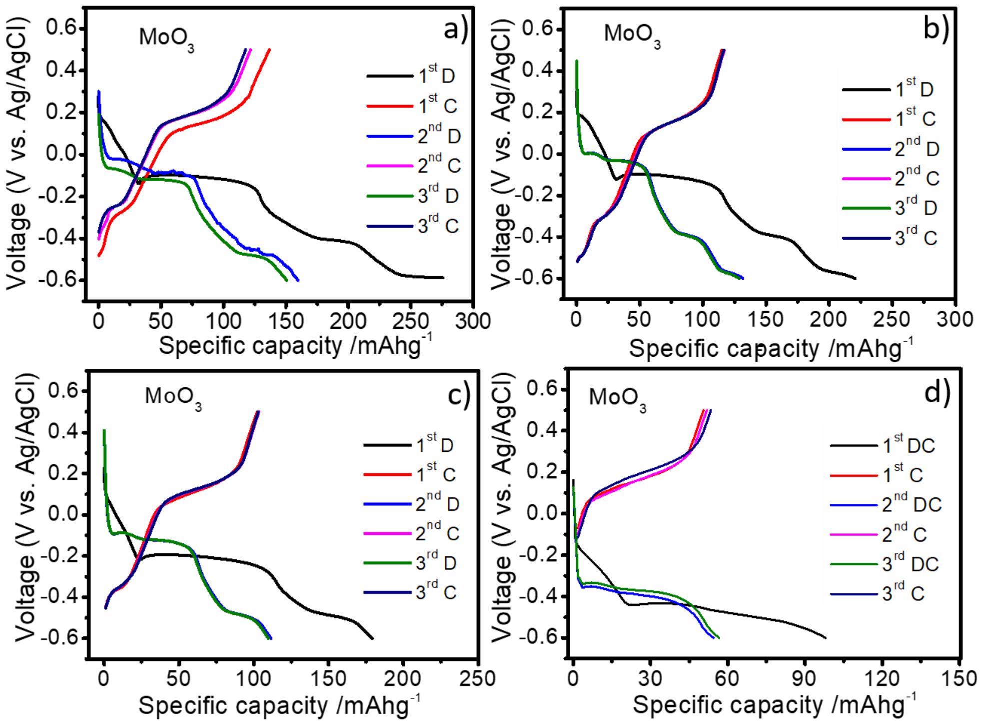

Figure 5.8 Galvanostatic charge discharge measurements of MoO_3 at current density of (a) 2 Ag^{-1}, (b) 5 Ag^{-1}, (c) 10 Ag^{-1} and (d) 20 Ag^{-1} in 1 M aqueous $AlCl_3$ electrolyte.

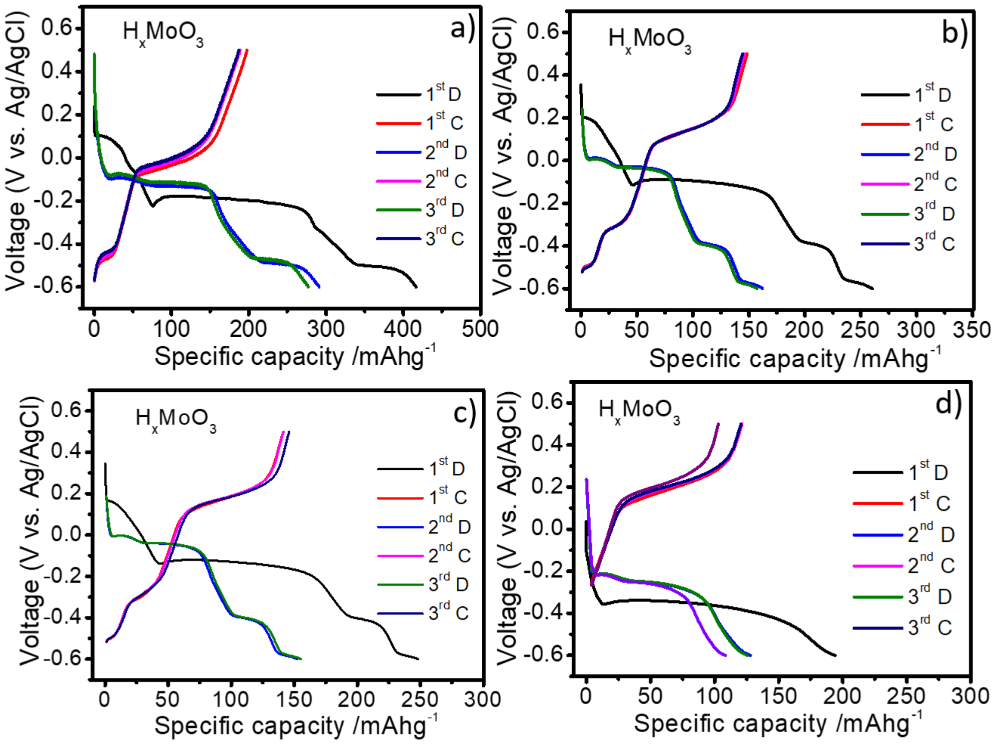

Figure 5.9. Galvanostatic charge discharge measurements of H_xMoO_3 at current density of (a) 2 Ag^{-1}, (b) 5 Ag^{-1}, (c) 10 Ag^{-1} and (d) 20 Ag^{-1} in 1 M aqueous $AlCl_3$ electrolyte.

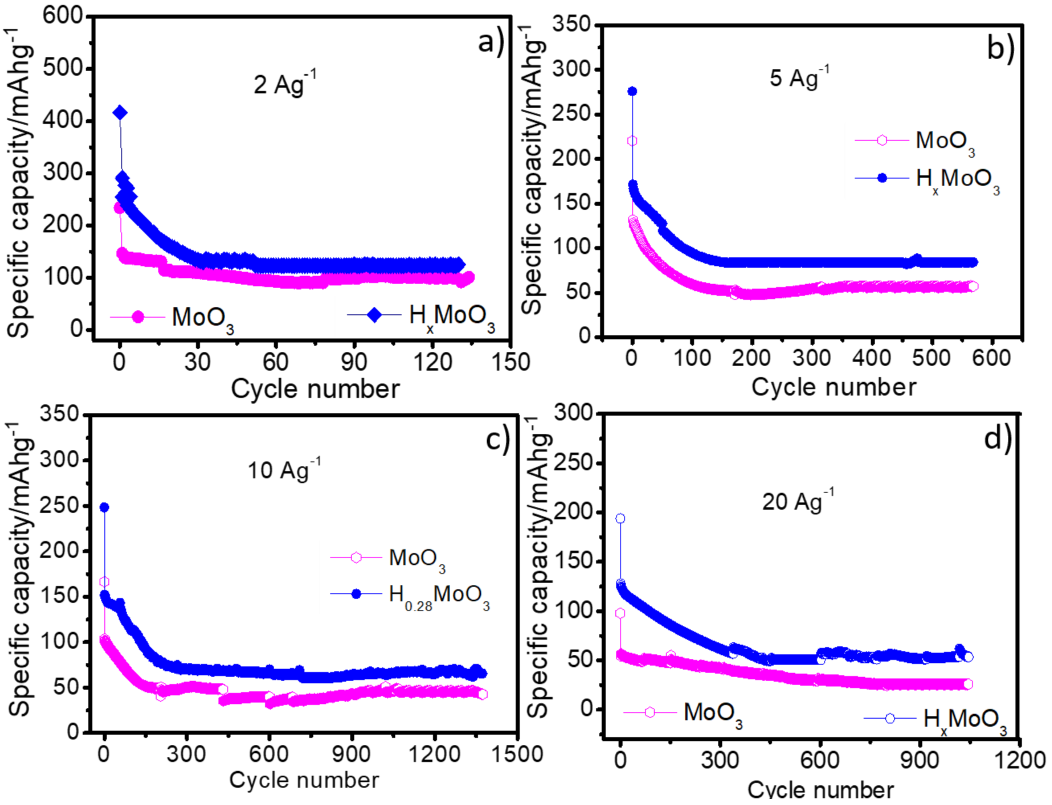

Figure 5.10. Rate performance of MoO_3 and H_xMoO_3 at current density of (a) 2 Ag^{-1}, (b) 5 Ag^{-1}, (c) 10 Ag^{-1} and (d) 20 Ag^{-1} in 1 M aqueous $AlCl_3$ electrolyte.

Electrolyte	**Current density**	**Phases**	**1st D (mAhg^{-1})**	**1st C (mAhg^{-1})**	**50th D (mAhg^{-1})**	**50th C (V) (mAhg^{-1})**
1 M $AlCl_3$	2 Ag^{-1}	MoO_3	274	137	105	76
		H_xMoO_3	417	196	132	120
	5 Ag^{-1}	MoO_3	221	115	80	73
		H_xMoO_3	260	148	120	100
	10 Ag^{-1}	MoO_3	180	103	80	70
		H_xMoO_3	247	140	119	100
	15 Ag^{-1}	MoO_3	174	90	80	74
		H_xMoO_3	224	120	112	102
	20 Ag^{-1}	MoO_3	97	50	50	46
		H_xMoO_3	193	119	107	102

Table 5.3 Specific Capacities after discharge and charge of MoO_3 and H_xMoO_3 at different current densities

Corroborating the CV profiles, the discharge-charge profiles of MoO_3 exhibit two distinct discharge potential plateaus at -0.15 V and -0.48 V at a current rate of 2 Ag^{-1} (Figure 5.8a). In fact, these potential plateaus are clearly visible even at higher current rates (up to 20 Ag^{-1}) (Figure 5.8(c,d)). At a current rate of 2 Ag^{-1}, MoO_3 shows a stable discharge capacity of around 100 mAg^{-1} over 130 cycles (Figure 5.8a). There is capacity decline at higher current rates and it is estimated to be around 25 $mAhg^{-1}$ over 1000 cycles at current rate of 20 Ag^{-1} (Figure 5.8(c,d)). Similarly, H_xMoO_3 also shows discharge plateaus at -0.21 V and -0.5 V at current of 2 Ag^{-1} (Figure 5.9a). However, a significant improvement in capacity could be noticed in this case in comparison to pristine MoO_3. The 1st discharge capacity is now 417 $mAhg^{-1}$, whereas it was 274 mAg^{-1} for MoO_3 (Figure 5.9 a and 5.10a). This enhancement in capacity continues over repeated cycling and around 37 % of increase could be noticed over 130 cycles (Figure 5.10a). Interestingly, H_xMoO_3 shows much better specific capacities even at higher current rates as shown in Figure 5.10 (b-d) and Table 5.3. For example, at a current rate of 10 Ag^{-1}, a discharge capacity of 105 $mAhg^{-1}$ after 130 cycles could be obtained for H_xMoO_3, which is approximately 90 % higher than that of pristine MoO_3 (Figure 5.10c). Additionally, the long-term stability test of H_xMoO_3 also shows enhancement compared to pristine MoO_3, as a stable discharge capacity of 54 mAh g^{-1} at a high current rate of 20 Ag^{-1} could be achieved over 1200 cycles (Figure 5.10d). The other important aspect is the reduction of polarization between the discharge and charge curves in the case of H_xMoO_3 (Figure 5.11 and Table 5.4). This indicates the facile transport of Al^{3+} ion in the structure of H_xMoO_3 due to H-doping. It is to be noted here that proton insertion may be a possibility. However, CV experiments performed in H_2SO_4 show that there is negligible possibility (Figure 5.12). Moreover, the galvanostatic charge-discharge experiments couldn't be completed at any current rates. It was also observed in our earlier work [20]. It is to be noted here that the overall structure of the nanobelts remain intact after repeated cycling as indicated by the ex-situ FESEM images (Figure 5.13).

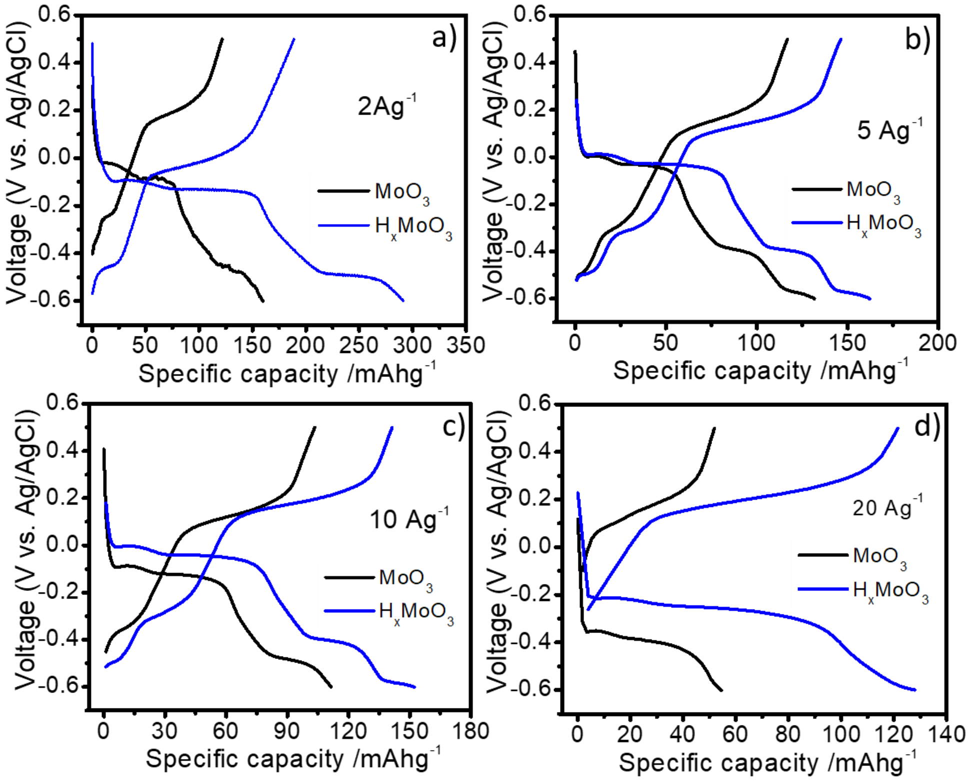

Figure 5.11 Comparison of 2nd cycle of galvanostatic charge discharge measurements of MoO_3 and H_xMoO_3 at current density of a) 2 Ag^{-1}, b) 5 Ag^{-1}, c) 10 Ag^{-1} and d) 20 Ag^{-1} in 1 M aqueous $AlCl_3$ electrolyte.

Electrolyte	Current density	Phases	Discharge(V)	Charge (V)	Peak Separations (V)
1 M $AlCl_3$	2 Ag^{-1}	MoO_3	-0.09	0.18	0.27
		H_xMoO_3	-0.13	-0.02	0.11
	5 Ag^{-1}	MoO_3	-0.08	0.15	0.23
		H_xMoO_3	-0.06	0.09	0.15
	10 Ag^{-1}	MoO_3	-0.16	0.11	0.27
		H_xMoO_3	-0.05	0.14	0.19
	15 Ag^{-1}	MoO_3	-0.19	0.19	0.38
		H_xMoO_3	-0.17	0.17	0.34
	20 Ag^{-1}	MoO_3	-0.4	0.16	0.56
		H_xMoO_3	-0.25	0.18	0.43

Table 5.4 Peak separation from GCD of MoO_3 and H_xMoO_3 at different current densities

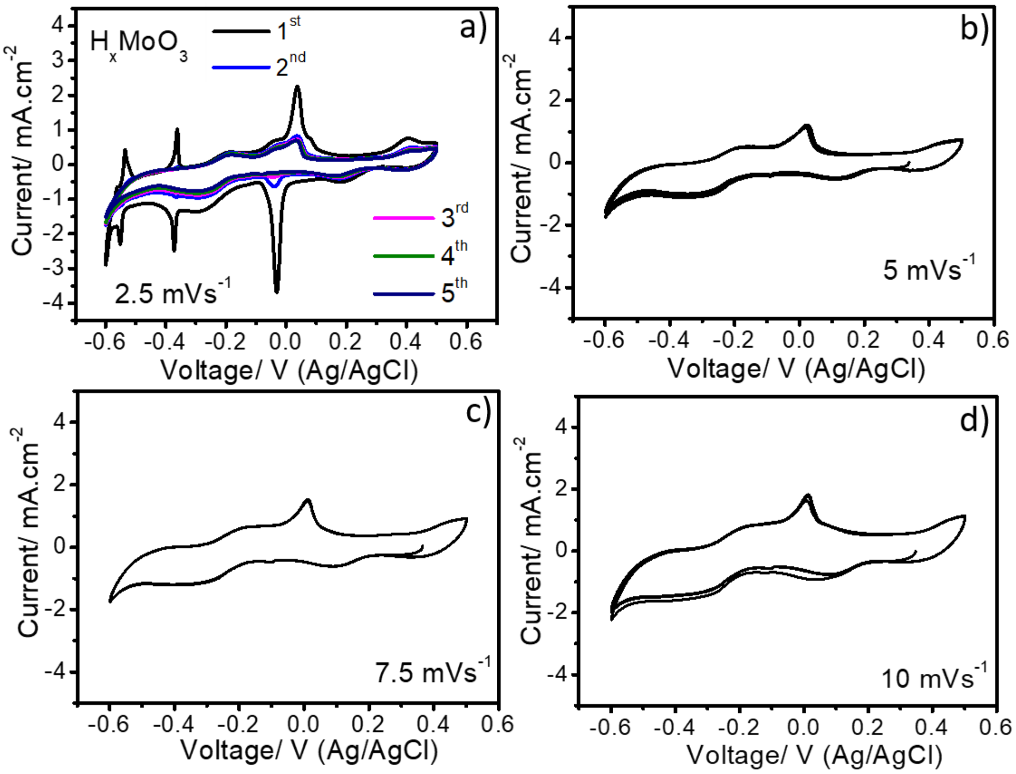

Figure 5.12 CV profile of H_xMoO_3 in 1 M H_2SO_4 aqueous electrolyte at different scan rates.

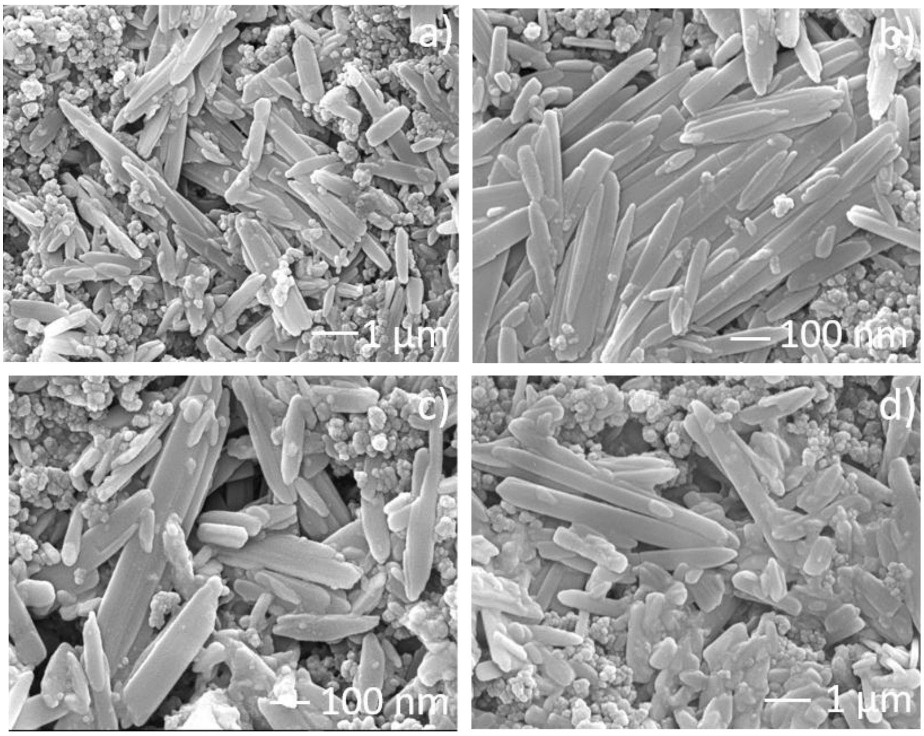

Figure 5.13. FESEM images of H_xMoO_3 after discharge.

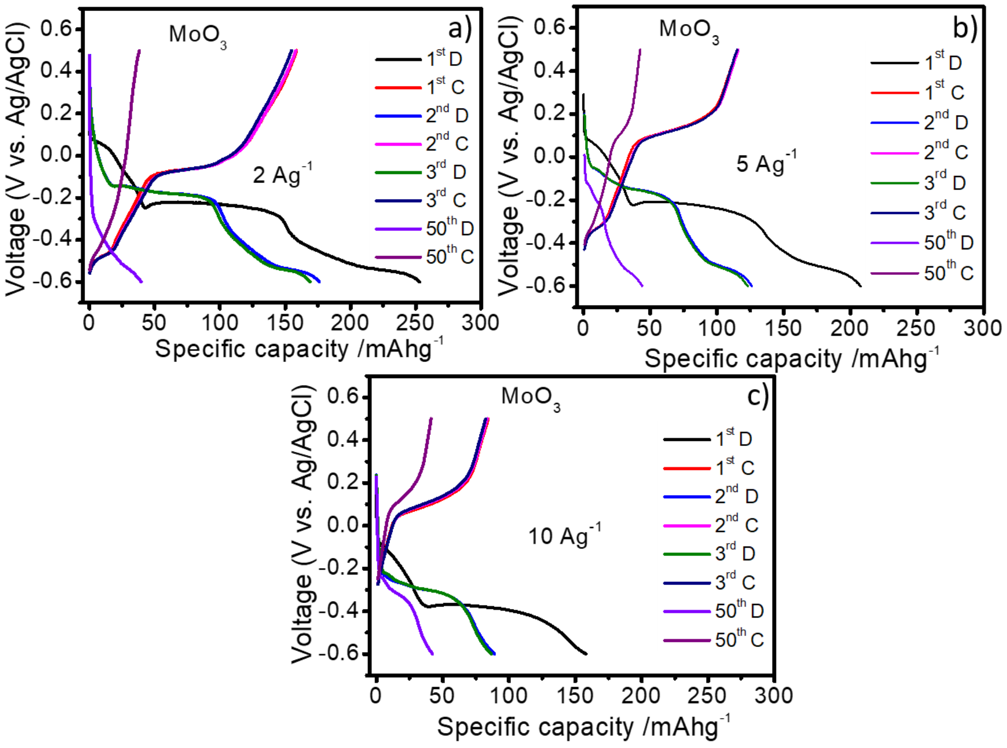

Figure 5.14. Galvanostatic charge discharge measurements of MoO_3 at current density of a) 2 Ag^{-1}, b) 5 Ag^{-1} and c) 10 Ag^{-1} in 0.5 M aqueous $Al_2(SO_4)_3$ electrolyte.

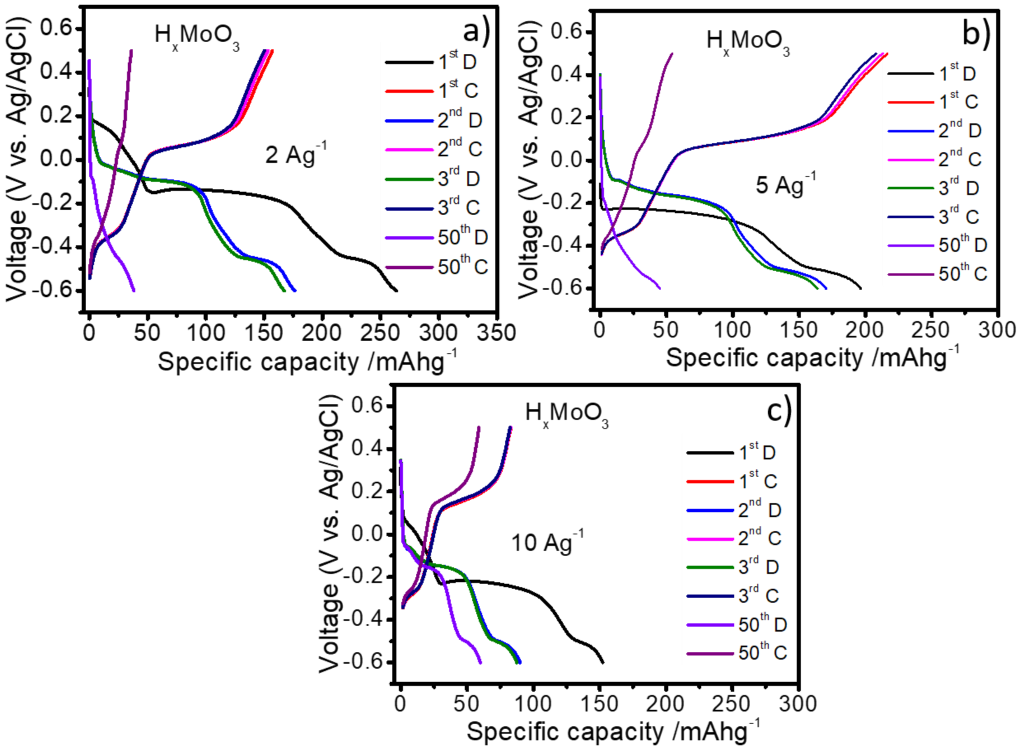

Figure 5.15. Galvanostatic charge discharge measurements of H_xMoO_3 at current density of a) 2 Ag^{-1}, b) 5 Ag^{-1} and c) 10 Ag^{-1} in 0.5 M aqueous $Al_2(SO_4)_3$ electrolyte.

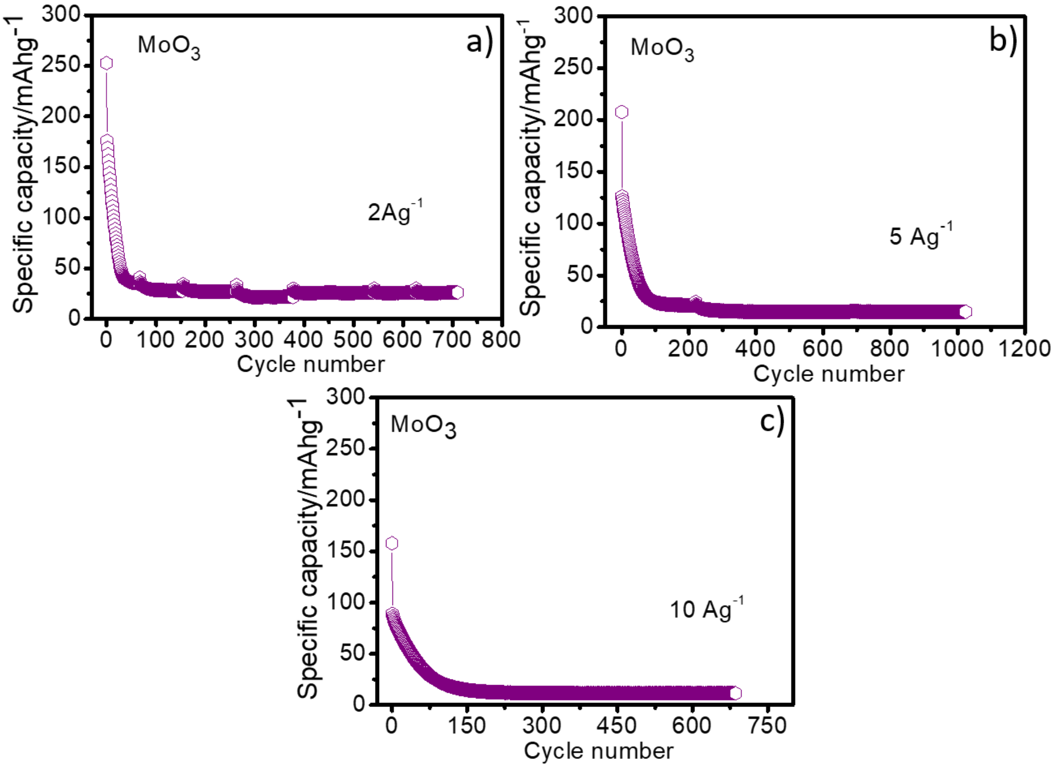

Figure 5.16. Rate performance of MoO_3 at current density of a) 2 Ag^{-1}, b) 5 Ag^{-1} and c) 10 Ag^{-1} in 0.5 M aqueous $Al_2(SO_4)_3$ electrolyte.

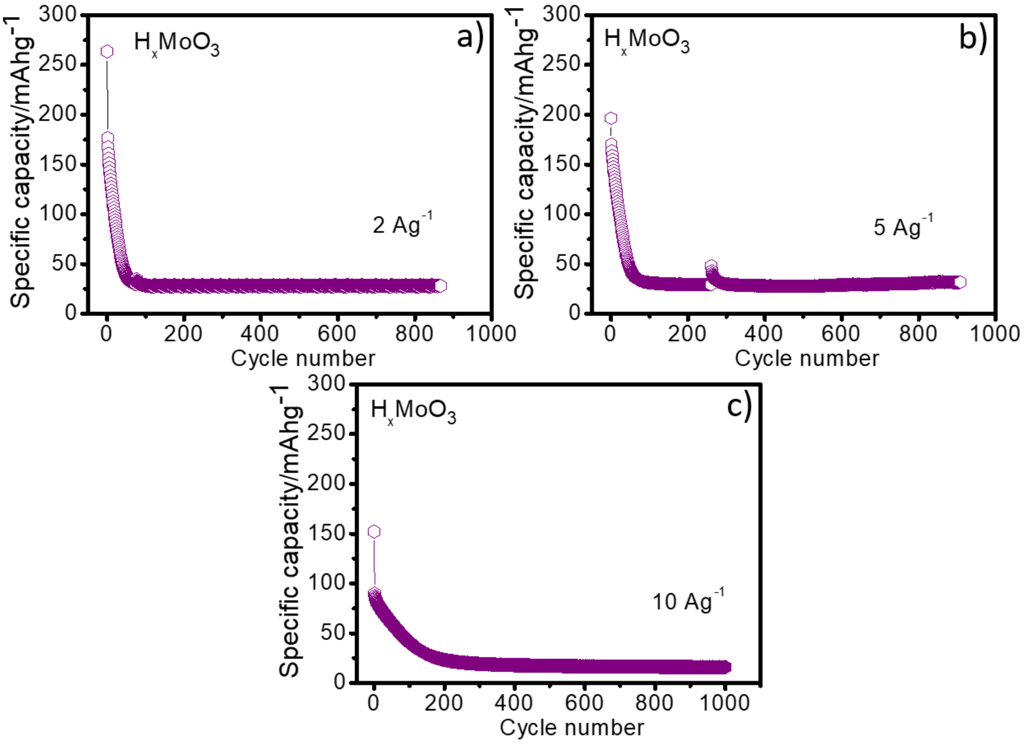

Figure 5.17. Rate performance of H_xMoO_3 at current density of a) 2 Ag^{-1}, b) 5 Ag^{-1} and c) 10 Ag^{-1} in 0.5 M aqueous $Al_2(SO_4)_3$ electrolyte.

In contrast, the charge discharge phenomena of MoO_3 and H_xMoO_3 shows serious capacity fading issue in $Al_2(SO_4)_3$ aqueous electrolyte from initial few cycles onwards (Figure 5. (14, 15)). The long-term cycling performance also degrades substantially at both lower and higher current densities, and nearly reaches zero with repeated cycling (Figure 5. (16,17)).

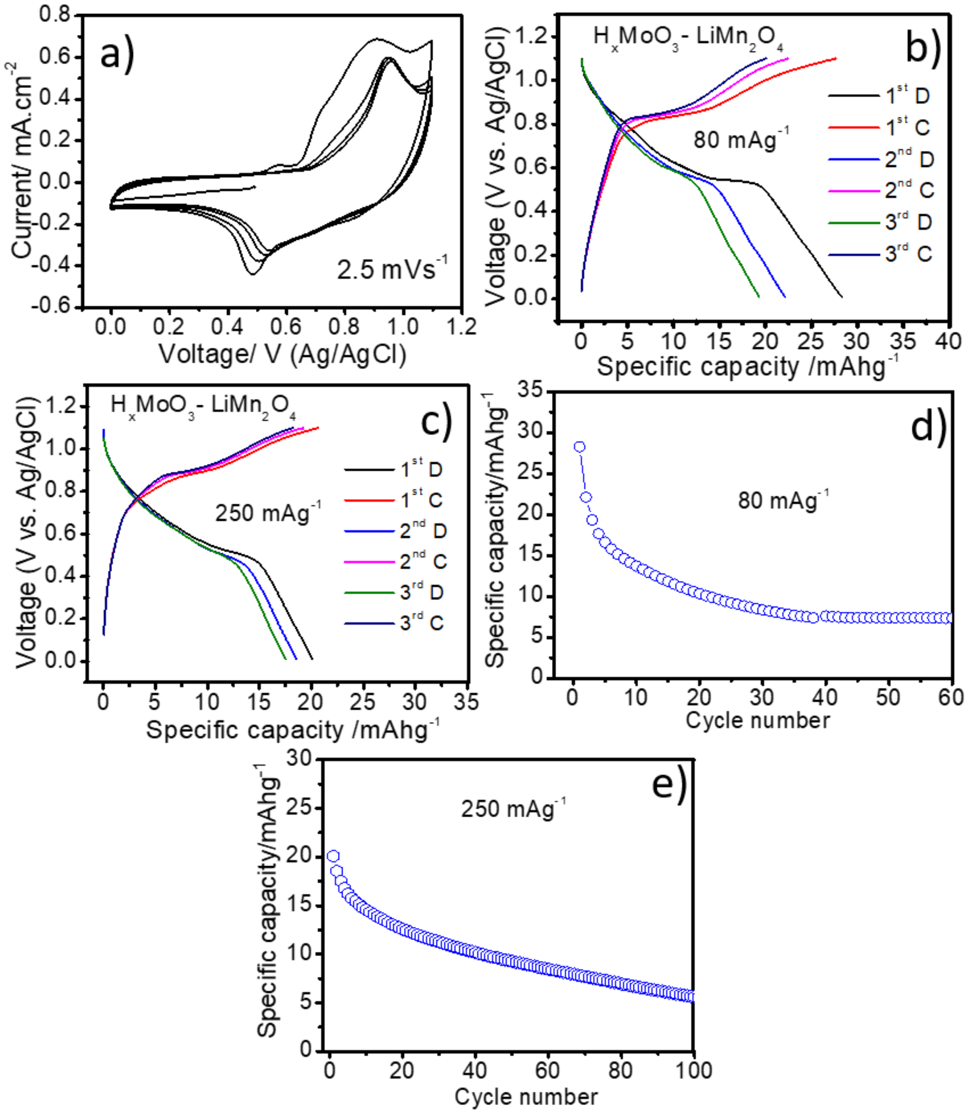

Figure 5.18. a) CV profile of the constructed $LiMn_2O_4$ // H_xMoO_3 cell at a scan rate of 2.5 mVs^{-1}. Galvanostatic charge-discharge measurements at current density of b) 80 mAg^{-1} and c) 250 mAg^{-1}, Rate performance at d) 80 mAg^{-1} and e) 250 mAg^{-1} of the constructed $LiMn_2O_4$ // H_xMoO_3 in 1 M aqueous $AlCl_3$ electrolyte.

Now, an assessment of an Al-ion cell was carried out considering $LiMn_2O_4$ and H_xMoO_3 as positive and negative electrode. Our earlier study on $LiMn_2O_4$ illustrated the Al^{3+} ion storage for Al-ion battery [32]. Figure 5.18a shows the cyclic voltammetry profile of the constructed cell in 1 M $AlCl_3$ aqueous electrolyte at 2.5 mVs^{-1}. Galvanostatic charge-discharge profiles indicate that there are short discharge and charge potential plateaus around 0.6 V and 0.8 V respectively. The initial discharge and charge capacities obtained are almost 28 mAhg^{-1} and 27 mAhg^{-1} respectively at a current density of 80 mAg^{-1} (Figure 5.18(b-e)).

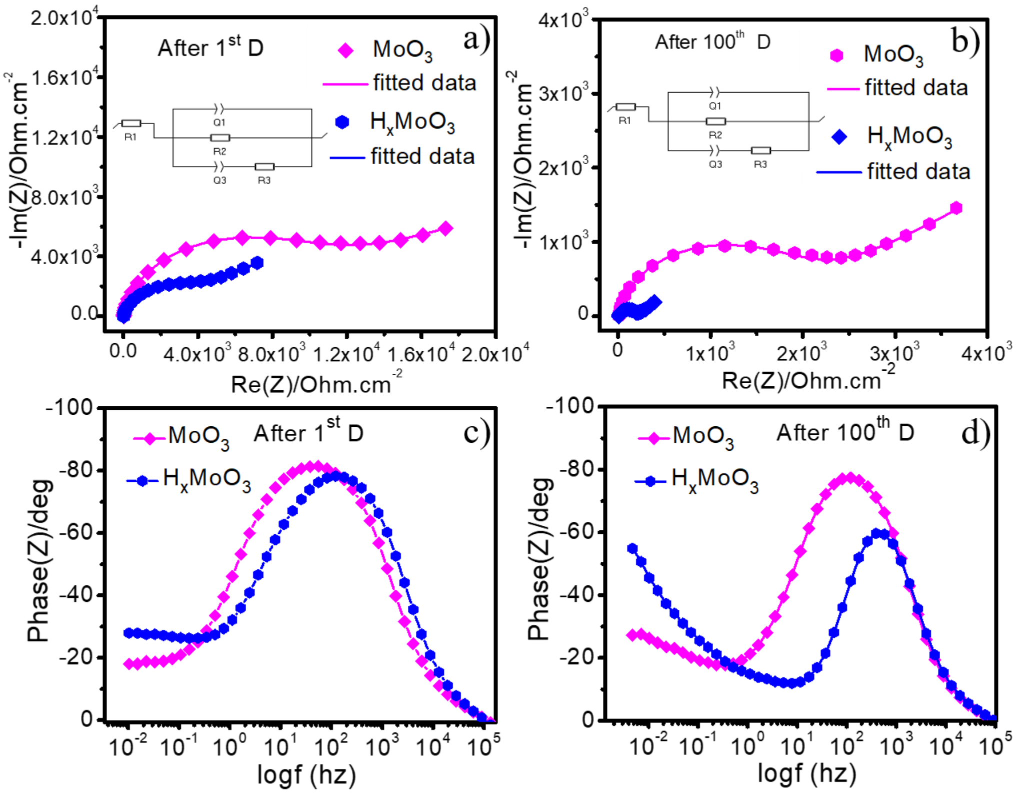

Figure 5.19 EIS spectra of MoO_3 and H_xMoO_3 after a)1st D and b)100th D; Bode plot after c)1st D and d)100th D.

Sl/ No	Phases	Discharge State	R_1 (Ohm.cm^{-2})	R_2 (Ohm.cm^{-2})	R_3 (Ohm.cm^{-2})
1	**MoO_3**	1D	Const	29435	4976
		100D	Const	10 683	1913
2	**H_xMoO_3**	1D	Const	14 170	2 968
		100D	Const	9 719	186.3

Table 5.5 Charge transfer resistance (R_3) values from EIS fitting.

To analyze the enhanced electrochemical performance in H_xMoO_3, the charge transfer resistances during the 1st and 100th discharge cycles in 1 M $AlCl_3$ aqueous electrolyte were evaluated using electrochemical impedance spectroscopy (EIS) technique. Figure 5.19 (a,b) show the EIS spectra of MoO_3 and H_xMoO_3 after 1st discharge state electrodes which are fitted against an equivalent circuit where R_1, R_2 and R_3 represent the solution, interface, and charge transfer resistance of the electrode respectively. The obtained charge transfer resistance values by fitting are shown in table 5.4. It is clearly evident from the EIS spectra that the semicircles in the higher frequency region corresponding to the MoO_3 electrode is larger than that of H_xMoO_3, indicating a higher charge transfer resistance for MoO_3 compared to H_xMoO_3 (Figure 5.19a). Interestingly, the EIS spectra recorded after the 100th discharge show a significant reduction in charge transfer resistance value for H_xMoO_3, highlighting its improved electrochemical performance in comparison to MoO_3 after hydrogen doping (Figure 5.19b). Notably, after 100th discharge, the charge transfer resistance of H_xMoO_3 is lower by a factor of 10 in comparison to pristine MoO_3 (Table 5.5). The Al^{3+} ion diffusion process was also further analyzed using the Bode plot as shown in figure 5.19(c, d). It is known that phase angle values in the lower frequency region can be corelated with the ion diffusion; i.e. smaller the phase angle faster is the ion diffusion rate [33]. From figure 5.19 (c,d) it is clearly observed that H_xMoO_3 has lower phase angle values than the MoO_3 after 1st and 100th discharged cycles.

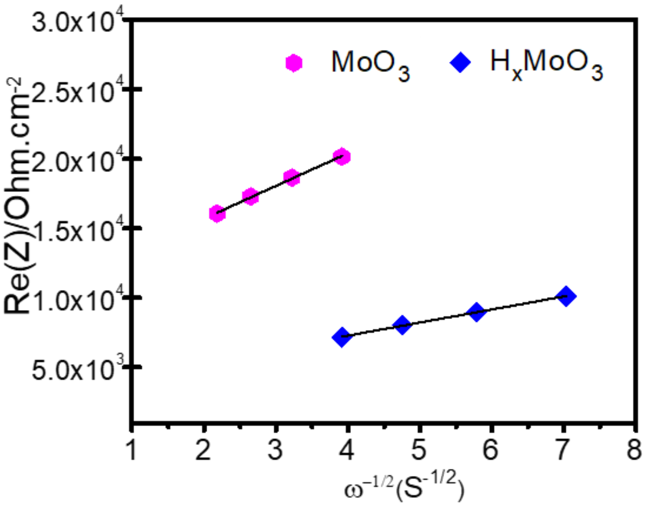

Figure 5.20 The relationship curve between Z′ and $\omega^{-1/2}$ in the low-frequency region.

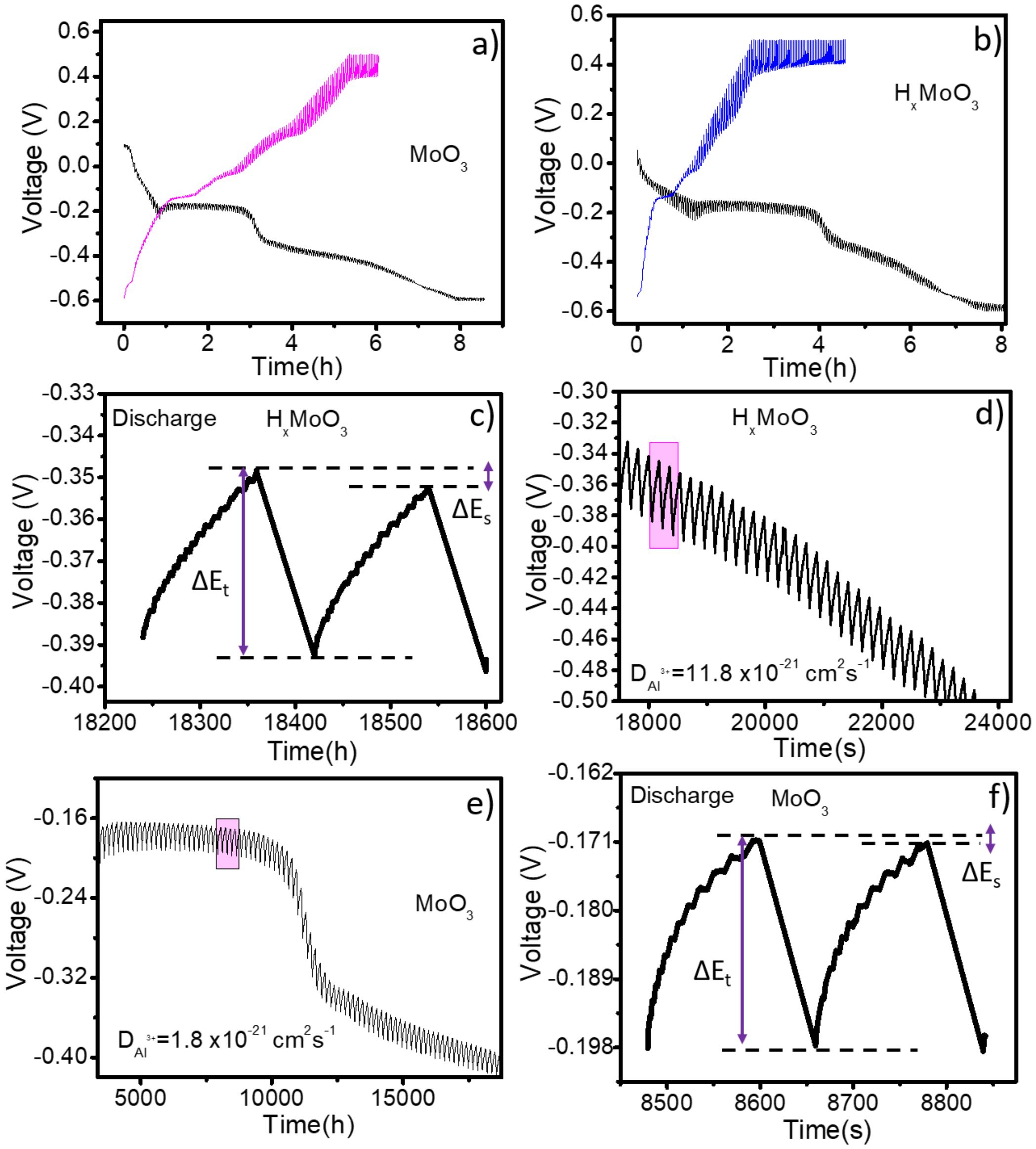

Figure 5.21. GITT profile of (a) MoO_3, (b) H_xMoO_3, during one complete charge/ discharge cycle at a current rate 0.1 $mAcm^{-2}$ (c) Demonstration of a single titration step during discharged state of H_xMoO_3, (d) enlarged view of one portion of the discharge curve with measured titration step highlighted on it; (e) GITT measurement of MoO_3 for one complete cycle, d) demonstration of a single titration step during discharged state of MoO_3.

The estimation of the diffusion coefficients from EIS data also supports the above findings since an enhanced diffusion was estimated for H_xMoO_3 in comparison to MoO^3 (Figure 5.20) [34,35]. The estimated diffusion coefficients are 1.25 x 10^{-21} cm^2s^{-1} and 7.9 x 10^{-21} cm^2s^{-1} for MoO_3 and H_xMoO_3 respectively. Further, it was also complemented by GITT measurements as shown in Figure 5.21 [36]. It was found that the diffusion coefficients are 11.72 x 10^{-21} cm^2s^{-1} and 1.8 x 10^{-21} cm^2s^{-1} for H_xMoO_3 and MoO_3 respectively.

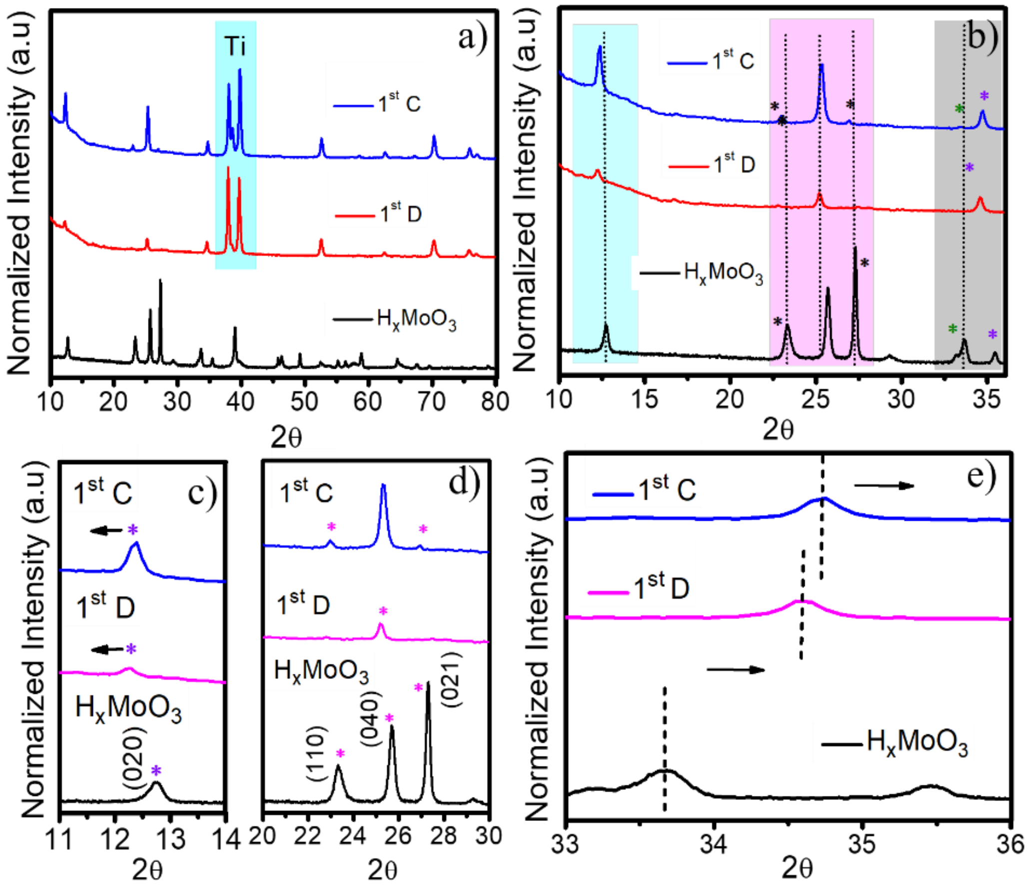

Figure 5.22 (a) XRD patterns of H_xMoO_3 after cycling, Enlarged view of the XRD patterns in the range of (b) 10°-35°, (c) 11°-13° (d) 20°-30° and (e) 33°-35° of discharged state electrode.

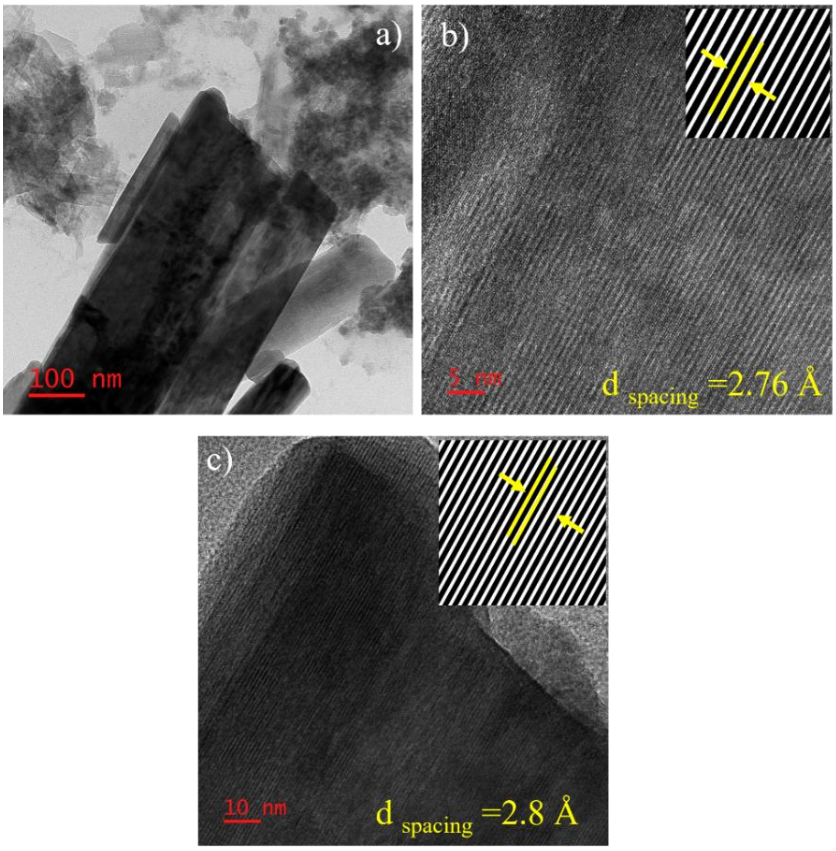

Figure 5.23 a-c) HRTEM and SAED pattern of discharged state electrode of H_xMoO_3 (D- discharge, C-charge).

The ex-situ XRD patterns of H_xMoO_3 after 1st discharge and 1st charge indicate the possible insertion of Al^{3+} ion (Figure 5.22). It could be seen that the (110) and (021) peaks at 23.2° and 27.25° disappear completely and the intensity of the (040) peak located at 25.7° decreases significantly. These diffraction peaks reappear again after charging (Figure 5.22d). Furthermore, the (020) peak at 12.7° is shifted by 0.42° towards lower diffraction angle after 1st discharge with concomitant shift to the higher angle side after charging (Figure 5.22c). Again, the peak at 33.6° shifts to higher angle by 0.92° (Figure 5.22e). Analysis of the HRTEM images of the discharged state electrode of H_xMoO_3 shows a fringe width of 2.76-2.8 Å signifying a possible contraction (Figure 5.23). Since the XRD pattern indicates both contraction and expansion, it is difficult to comment on the discharged state electrode due to its inherent complexity.

5.5 Conclusion

In conclusion, the Al^{3+} ion storage properties of H_xMoO_3 are illustrated which show significant reduction of polarization and enhancement in the specific capacities at higher current rates. Various morphological and structural analysis suggest presence of hydrogen ion in the MoO_3 lattice structure. Interestingly it is observed that insertion of hydrogen in the MoO_3 structure leads to the subtle contraction of the crystal planes of MoO_3. MoO_3 shows a stable discharge capacity of around 100 mAg^{-1}, although there is capacity decline at higher current rates. However, a significant improvement in capacity could be noticed in H_xMoO_3 in comparison to pristine MoO_3. The 1st discharge capacity is now 417 $mAhg^{-1}$, whereas it was 274 mAg^{-1} for MoO_3. At higher current rates H_xMoO_3 shows much better specific capacities as a stable discharge capacity of 54 mAh g^{-1} at a high current rate of 20 Ag^{-1} could be achieved over 1200 cycles. From the EIS and bode analysis it can be predicted that H_xMoO_3 shows improved charge transfer phenomena. An enhanced diffusion rate could also be estimated where diffusion rate is enhanced by almost a factor of 7 in case of H_xMoO_3 in comparison to pristine MoO_3. Ex-situ XRD and HRTEM analysis predicts possible contraction and expansion of crystal planes of H_xMoO_3 after Al^{3+} ion insertion.

5.6 References

[1] Tian, Y., Zeng, G., Rutt, A., Shi, T., Kim, H., Wang, J., Koettgen, J., Sun, Y., Ouyang, B., Chen, T. and Lun, Z. Promises and challenges of next-generation beyond Li-ion batteries for electric vehicles and grid decarbonization. *Chemical reviews*, 121(3): 1623-1669, 2020.

[2] Tarascon, J.M. and Armand, M. Issues and challenges facing rechargeable lithium batteries. *Nature*, 414(6861): 359-367, 2001.

[3] Etacheri, V., Marom, R., Elazari, R., Salitra, G. and Aurbach, D. Challenges in the development of advanced Li-ion batteries: a review. *Energy & environmental science*, 4(9):3243-3262, 2011.

[4] Arico, A.S., Bruce, P., Scrosati, B., Tarascon, J.M. and Van Schalkwijk, W. Nanostructured materials for advanced energy conversion and storage devices. *Nature materials*, 4(5): 366-377, 2005.

[5] Wang, L.P., Yu, L., Wang, X., Srinivasan, M. and Xu, Z.J. Recent developments in electrode materials for sodium-ion batteries. *Journal of Materials Chemistry A*, 3(18): 9353-9378, 2015.

[6] Jache, B. and Adelhelm, P. Use of graphite as a highly reversible electrode with superior cycle life for sodium-ion batteries by making use of co-intercalation phenomena. *Angewandte Chemie International Edition*, *53*(38): 10169-10173, 2014.

[7] Fang, S., Bresser, D. and Passerini, S. Transition metal oxide anodes for electrochemical energy storage in lithium-and sodium-ion batteries. *Transition Metal Oxides for Electrochemical Energy Storage*: 55-99, 2022.

[8] Shin, S., Yoon, J., Kim, E., Yoon, W.S. and Shin, H. High capacity and reversibility of oxygen-vacancy-controlled MoO_3 on Cu in Li-ion batteries: unveiling storage mechanism in binder-free MoO_{3-x} anodes. *Energy Technology*, 8(6): 1901502, 2020.

[9] Ma, F., Yuan, A., Xu, J. and Hu, P., 2015. Porous α-MoO_3/MWCNT nanocomposite synthesized via a surfactant-assisted solvothermal route as a lithium-ion-battery high-capacity anode material with excellent rate capability and cyclability. *ACS applied materials & interfaces*, 7(28): 15531-15541, 2015.

[10] Chen, J.S., Cheah, Y.L., Madhavi, S. and Lou, X.W. Fast synthesis of α-MoO_3 nanorods with controlled aspect ratios and their enhanced lithium storage capabilities. *The Journal of Physical Chemistry C*, 114(18): 8675-8678, 2010.

[11] Zhang, H., Gao, L. and Gong, Y. Exfoliated MoO_3 nanosheets for high-capacity lithium storage. *Electrochemistry Communications*, 52: 67-70, 2015.

[12] Zhou, L., Yang, L., Yuan, P., Zou, J., Wu, Y. and Yu, C.α-MoO_3 nanobelts: a high-performance cathode material for lithium-ion batteries. *The Journal of Physical Chemistry C*, 114(49): 21868-21872, 2010.

[13] Zhang, Y., Dong, X., Li, H., Xu, S., Li, R., Zeng, S., Fu, C. and Wang, L. Study for the enhanced energy storage properties of α-MoO_3 microstructures in lithium-ion batteries. *CrystEngComm*, 24(22): 4041-4048, 2022.

[14] Li, Y., Sun, H., Cheng, X., Zhang, Y. and Zhao, K. In-situ TEM experiments and first-principles studies on the electrochemical and mechanical behaviors of α-MoO_3 in Li-ion batteries. *Nano Energy*, 27: 95-102, 2016.

[15] Meduri, P., Clark, E., Kim, J.H., Dayalan, E., Sumanasekera, G.U. and Sunkara, M.K. MoO_{3-x} nanowire arrays as stable and high-capacity anodes for lithium-ion batteries. *Nano letters*, 12(4): 1784-1788, 2012.

[16] Wu, K., Zhan, J., Xu, G., Zhang, C., Pan, D. and Wu, M. MoO_3 nanosheet arrays as superior anode materials for Li-and Na-ion batteries. *Nanoscale*, 10(34): 16040-16049, 2018.

[17] Wang, B., Ang, E.H., Yang, Y., Zhang, Y., Geng, H., Ye, M. and Li, C.C. Interlayer engineering of molybdenum trioxide toward high-capacity and stable sodium ion half/full batteries. *Advanced Functional Materials*, 30(28): 2001708, 2020.

[18] Pan, Z., Liu, X., Yang, J., Li, X., Liu, Z., Loh, X.J. and Wang, J. Aqueous rechargeable multivalent metal-ion batteries: advances and challenges. *Advanced Energy Materials*, 11(24): 2100608, 2021.

[19] Tang, X., Zhou, D., Zhang, B., Wang, S., Li, P., Liu, H., Guo, X., Jaumaux, P., Gao, X., Fu, Y. and Wang, C. A universal strategy towards high–energy aqueous multivalent–ion batteries. *Nature communications*, 12(1): 2857, 2021.

[20] Lahan, H. and Das, S.K. Al^{3+} ion intercalation in MoO_3 for aqueous aluminum-ion battery. *Journal of power sources*, 413: 134-138, 2019.

[21] Joseph, J., O' Mullane, A.P. and Ostrikov, K. Hexagonal molybdenum trioxide (h-MoO_3) as an electrode material for rechargeable aqueous aluminum-ion batteries. *ChemElectroChem*, 6(24): 6002-6008, 2019.

[22] Chung, S.Y., Bloking, J.T. and Chiang, Y.M. Electronically conductive phospho-olivines as lithium storage electrodes. *Nature materials*, 1(2): 123-128, 2002.

[23] Fang, Y., Yu, X.Y. and Lou, X.W. Formation of hierarchical Cu-doped $CoSe_2$ microboxes via sequential ion exchange for high-performance sodium-ion batteries. *Advanced materials*, 30(21): 1706668, 2018.

[24] Ju, X., Ning, P., Tong, X., Lin, X., Pan, X., Li, Q., Duan, X. and Wang, T. H_xMoO_3 nanobelts with better performance as anode in lithium-ion batteries. *Electrochimica Acta*, 213: 641-647, 2016.

[25] Ou, J.Z., Campbell, J.L., Yao, D., Wlodarski, W. and Kalantar-Zadeh, K. In situ Raman spectroscopy of H_2 gas interaction with layered MoO_3. *The Journal of Physical Chemistry C*, 115(21): 10757-10763, 2011.

[26] Maheswari, N. and Muralidharan, G. Controlled synthesis of nanostructured molybdenum oxide electrodes for high performance supercapacitor devices. *Applied surface science*, 416: 461-469, 2017.

[27] Hu, X.K., Qian, Y.T., Song, Z.T., Huang, J.R., Cao, R. and Xiao, J.Q. Comparative study on MoO_3 and H_xMoO_3 nanobelts: structure and electric transport. *Chemistry of materials*, 20(4): 1527-1533, 2008.

[28] Hu, X., Ma, D., Xu, L., Zhu, Y. and Qian, Y. Selective Preparation of MoO_3 and H_xMoO_3 Nanobelts in Molybdenum–Hydrogen Peroxide System. Chemistry *letters*, 35(8): 962-963, 2006.

[29] Ju, X., Ning, P., Tong, X., Lin, X., Pan, X., Li, Q., Duan, X. and Wang, T. H_xMoO_3 nanobelts with better performance as anode in lithium-ion batteries. *Electrochimica Acta*, 213: 641-647, 2016.

[30] Amba Sankar, K.N., Kesavan, L., Saha, B., Jyolsnaraj, M.K., Mohan, S., Nandakumar, P., Mohanta, K. and Kvarnström, C. Renewable synthesis of MoO3 nanosheets via low temperature phase transition for supercapacitor application. *Scientific Reports*, 14(1): 20503, 2024.

[31] Kumar, R., Mishra, V., Dixit, T., Sarangi, S.N., Samal, D., Miryala, M., Nayak, P.K. and Rao, M.S. Investigating the effect of H+-ion irradiation on layered α-MoO_3 flakes by defect engineering. *Applied Physics Letters*, 123(15): 2023.

[32] Nandi, S. and Das, S.K., 2021. An electrochemical study on $LiMn_2O_4$ for Al^{3+} ion storage in aqueous electrolytes. *Physical Chemistry Chemical Physics*, 23(35): 19150-19154.

[33] Wang, D.W., Li, F., Fang, H.T., Liu, M., Lu, G.Q. and Cheng, H.M. Effect of pore packing defects in 2-D ordered mesoporous carbons on ionic transport. *The Journal of Physical Chemistry B*, 110(17): 8570-8575, 2006.

[34] An, C., Yuan, Y., Zhang, B., Tang, L., Xiao, B., He, Z., Zheng, J. and Lu, J. Graphene wrapped $FeSe_2$ nano-microspheres with high pseudocapacitive contribution for enhanced Na-ion storage. *Advanced Energy Materials*, 9(18): 1900356, 2019.

[35] Qin, J., Sari, H.M.K., Wang, X., Yang, H., Zhang, J. and Li, X. Controlled design of metal oxide-based (Mn^{2+}/Nb^{5+}) anodes for superior sodium-ion hybrid supercapacitors: Synergistic mechanisms of hybrid ion storage. *Nano Energy*, 71: 104594, 2020.

[36] Dees DW, Kawauchi S, Abraham DP, Prakash J. Analysis of the Galvanostatic Intermittent Titration Technique (GITT) as applied to a lithium-ion porous electrode. *Journal of Power Sources*.189(1): 263-8, 2009.